JST: Engineering and Technology for Sustainable Development
Volume 33, Issue 5, November 2023, 009-018

Effect of Nozzle Travel Path Strategies on the Mechanical Properties of Inconel 625 Superalloy Parts Formed by Direct Laser Metal Deposition

Duong.Van Nguy, Trinh. Quang Hung, Doan.Tat Khoa*
Military Technical Academy, Ha Noi, Vietnam
**Corresponding author email: khoadt@lqdt.edu.vn*

Abstract

To reduce the occurrence of cracks in the Inconel 625 nickel-based super-alloy during the Direct Laser Metal Deposition (DLMD) process, this study simulated the temperature and stress fields of thin-walled parts. The model was used to determine the effect of nozzle travel path strategies (single direction and reverse direction) on the final stress distribution, and compared the differences in residual stress distribution within the thin-walled part. The results showed that with the single direction scanning method, the residual stress at both ends of the thin-walled part was relatively high while the stress at the middle was smaller, with a stress difference between the maximum and minimum of about 900 MPa. In contrast, with the reverse direction scanning method, the residual stress in the thin-walled part was distributed relatively evenly, with a stress difference of about 300 MPa between both ends and the center. The experimental results showed that with the single direction scanning method, cracks occurred at both ends and in the middle of the thin-walled part, whereas with the reverse direction scanning method, warping and cracks phenomena were eliminated. The microstructure of the Inconel 625 in the forming layer is characterized by a columnar crystal structure that has a small length and grows perpendicularly to the scanning direction. This growth is continuous between the forming layers. In both cases, the micro-hardness increases with the height of the formed layers; the microhardness values in the left, right, and middle regions are relatively uniform, the microhardness measurement values range from 420 to 450 HV.

Keywords: Direct laser metal deposition, nozzle travel path strategies, thin-wall, residual stress, crack.

1. Introduction

Inconel 625, a nickel-based superalloy, is the main material for forming aircraft engine parts such as turbine blades and stiffeners. They are difficult to fabricate using traditional casting and forging methods. Therefore, the use of Direct Laser Metal Deposition (DLMD) to form thin-walled Inconel 625 components will have a significant impact on the development of the aviation and aerospace industry [1-3]. Inconel 625 is a multi-component superalloy, and the melting points of each element differ significantly. During the forming process, the local part of the component is rapidly heated and then cooled, which cannot make the composition diffuse uniformly. As a result, the chemical composition inside each grain is uneven, resulting in significant stress concentration. Under the thermal stress generated during the solidification process, cracks occur and propagate at the grain boundaries. Cracking of the cladding layer directly affects the quality of the component [4].

In previous research on DLMD, various methods have been used to solve the component cracking during forming. The primary methods include adjusting the material composition to increase plasticity [5], optimizing the process parameters [6], utilizing multiple process composite manufacturing [7], preheating the substrate [8], post-forming heat treatment, and reducing the oxygen content in the protective atmosphere [9]. Although these studies have been effective in reducing cracking during DLMD, there are few publications detailing the stress distribution, crack morphology, and crack distribution of Inconel 625 components formed by DLMD.

The purpose of this paper is to investigate the influence of the scanning method on the distribution of stress, formation of cracks, microstructure, and microhardness of thin-walled components fabricated from Inconel 625 material using DLMD technology.

2. Numerical Simulation

2.1. Establishing Model

The temperature and stress fields of metal thin-walled parts formed by DLMD using ANSYS "Death and Birth element" technique were studied. In the forming process, Inconel 625 powder is utilized as the forming material, with its material composition detailed in Table 1, supplied by Sandvik [10]. The substrate material employed is 316L stainless steel, with its material composition outlined in Table 2, supplied by thyssenkrupp Materials [11]. The

---

ISSN 2734-9381
https://doi.org/10.51316/jst.170.etsd.2023.33.5.2
Received: April 5, 2023; accepted: July 8, 2023

dimensions of the thin-walled model are shown in Fig. 1(a), with a substrate size of 30 mm × 10 mm × 3 mm and a cladding layer size of 20 mm × 0.5 mm × 1 mm (consisting of 10 layers). To reduce computational complexity, a finer regular mapped mesh was used for the cladding layer, while a coarser hexahedral mesh and tetrahedral mesh were used for the substrate and the transition between the substrate and the part, respectively, as shown in Fig. 2.

Table 1. Composition of Inconel 625 powder (wt%).

Ni	Cr	Fe	Mo	Nb+Ta	C	Mn
>58	20-23	<5	8-10	3.15-4.15	<0.1	<0.5
Si	P	S	Al	Ti	Co	
<0.5	<0.015	<0.015	<0.4	<0.4	<1	

Table 2. Composition of 316L substrate (wt%).

C	Cr	Ni	Si	Mn	Mo	P	S	Fe
≤0.03	16.5-18.5	10-13	1.0	2.0	2.0-2.5	0.045	0.015	Bal

Table 3. Process parameters.

Laser power (W)	Scanning speed (mm/s)	Powder feeding rate (g/min)	Laser diameter (mm)	Initial temperature (°C)
250	10	2.8	0.5	20

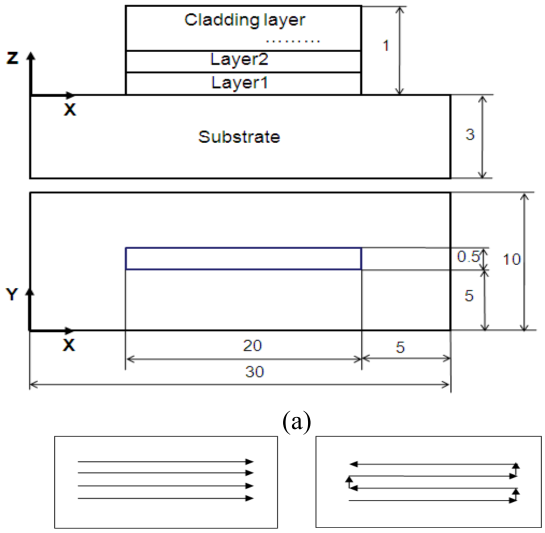

(a)

(b)

(c)

Fig. 1. Schematic presentation of scanning method. (a) model; (b) single direction of scanning; (c) reverse direction of scanning.

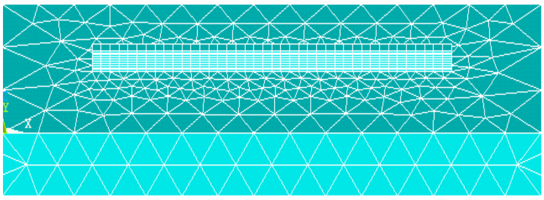

Fig. 2. Finite element model of the substrate and cladding layer.

The substrate elements used SOLID98 tetrahedral coupled elements with ten nodes, while the cladding layer elements used SOLID5 hexahedral coupled elements with eight nodes. The process parameters are shown in Table 3. The initial temperature of the substrate was 20 °C, which is the ambient temperature, and the boundary condition is convective heat transfer. The latent heat treatment is assumed to vary with temperature, and the activated element pool has no convective heat transfer at the melting temperature. The stress at the beginning of the process is assumed to be free stress, and the reference temperature of the substrate and cladding material is the ambient temperature and the melting temperature, respectively. One element is activated every 0.05 seconds, with a heat flow area of 0.5 mm × 0.5 mm. Finally, different scanning methods are defined by activating the corresponding elements, as shown in Fig. 1(b) and Fig. 1(c).

As mentioned, the laser beam in the DLMD process strikes the substrate and melts the powder particles. The bead is formed continuously by moving the laser beam over the surface. The temperature field is calculated by solving the 3D heat conduction moving heat source equation shown in the following equation [12]:

$$\rho c_p \frac{\partial T}{\partial t} - \rho c_p \nabla(UT) - \nabla.(K\nabla T) = Q \qquad (1)$$

where ρ, c_p, and K are the density, heat capacity, and thermal conductivity, respectively. U is the heat source speed and Q is the heat generation that is not considered in this analysis. As mentioned with the finite element method, the moving heat source is not directly considered. However, the continuous addition of the material to the substrate is divided into many small time steps, and for each time step, a stationary heat transfer equation is solved. The APDL subroutine defines the position of the laser beam at a given time step as a function of U and the beam diameter:

$$\rho c_p \frac{\partial T}{\partial t} - \nabla.(K\nabla T) = Q \qquad (2)$$

Therefore, (1) is simplified to form (2) and should be solved for each time step with its corresponding boundary conditions.

The boundary conditions are:

$$-K(\nabla T.n)|_{\xi} = \begin{cases} -h(T - T_0) - \varepsilon\sigma(T^4 - T_0^4) \\ -h(T - T_0) \end{cases} \quad (3)$$

where h is the convection heat transfer, and ε and σ are the radiation coefficient and Stephen Boltzmann constant, respectively. The shielding gas effect beside the radiation from the molten pool is considered in the boundary condition of the molten pool. All sides of the substrate have a convection heat transfer boundary condition. The following conditions should be also satisfied:

$$T(x, y, z, 0) = T(x, y, z, \infty) = T_0 \quad (4)$$

The material properties are defined to be temperature dependent, and the latent heat of fusion is considered in the definition of specific heat.

The total strain can be written as the sum of the individual components of the strain:

$$\varepsilon_{kl} = \varepsilon_{kl}^{E} + \varepsilon_{kl}^{P} + \varepsilon_{kl}^{T} \quad (5)$$

k,l =1,2,3

where ε^E, ε^P, and ε^T are the elastic, plastic, and thermal strains, respectively. The transformation plasticity and volume dilatation strains are not considered in this model.

2.2. Temperature and Stress Fields Analysis

2.2.1. Temperature fields

The temperature distribution after completing the tenth layer of the thin-walled part under two different scanning methods is shown in Fig. 3.

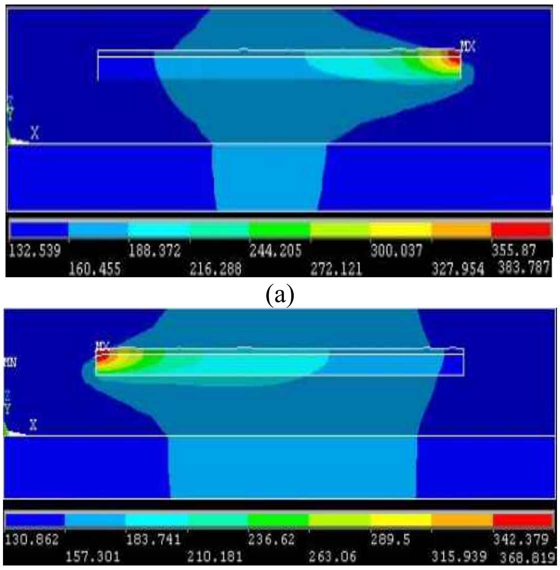

(a)

(b)

Fig. 3. Temperature distribution of the cladding layer after the last deposition step. (a) single direction of scanning; (b) reverse direction of scanning.

As depicted, the temperature gradient varies between the two scanning methods due to their unique characteristics. In the single direction scanning method, the laser beam scans one layer and then pauses for one second before moving up in the *Z* direction, returning to the starting point, and then beginning to scan the next layer. This leads to a longer cooling time for the previous layer, resulting in a larger temperature gradient of the cladding layer. On the other hand, in the reverse direction scanning method, the laser beam scans one layer, pauses for one second, moves up in the *Z* direction, and immediately scanning the next layer begins. The shorter cooling time of the previous layer results in a smaller temperature gradient, which is similar to preheating the substrate.

2.2.2. Stress fields

a) Stress in three directions under single direction scanning method.

Fig. 4 shows the distribution of stress in the *X*, *Y*, and *Z* directions of the thin-walled layer under the single direction scanning method. Specifically, Fig. 4(a) depicts the stress distribution in the *X* direction (parallel to the scanning direction) under the single direction scanning method. The middle section of the thin-walled part experiences tensile stress, with the direction of the stress along the scanning direction (from left to right). The stress values are relatively large (400 to 900 MPa) and tend to decrease along the scanning direction. Moreover, along the height of the cladding layer, the stress increases and is mainly concentrated on the left side of the middle.

Fig. 4(b) shows the stress distribution in the *Y* direction (thickness direction) under the single direction scanning method. The stress distribution in the middle is relatively uniform, with stress values ranging from -30 MPa to 20 MPa. The stress at the left end is compressive stress, with a stress value of about -600 MPa, whereas the stress at the right end is tensile stress, with a stress value of about 800 MPa.

Fig. 4(c) shows the stress distribution in the *Z* direction (perpendicular to the scanning direction) under the single direction scanning method. The stress distribution in the middle is relatively uniform, and along the height of the thin-walled part, the stress tends to increase and changes from compressive stress to tensile stress. However, the stress values are relatively small, ranging from -80 MPa to 50 MPa.

The stress in the *X* direction is greater than that in the *Y* and *Z* directions, and the total stress at the node results from the combination of stresses in all three directions. The main stress at the node of the thin-walled part is the stress in the *X* direction.

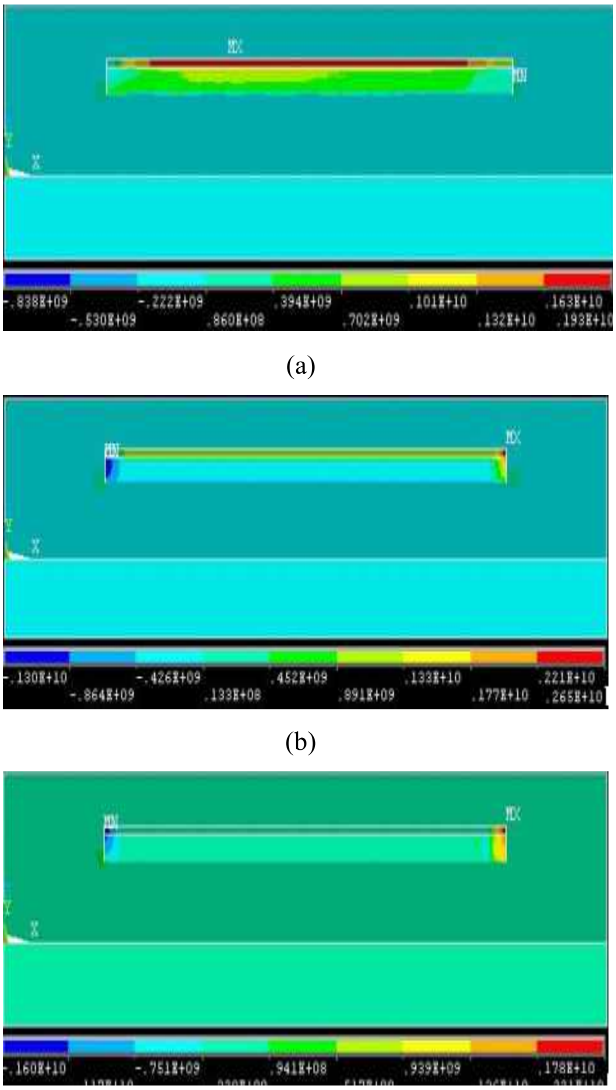

(a)

(b)

(c)

Fig. 4. Single direction of scanning of stress distribution. (a) *X* stress distribution; (b) *Y* stress distribution; (c) *Z* stress distribution.

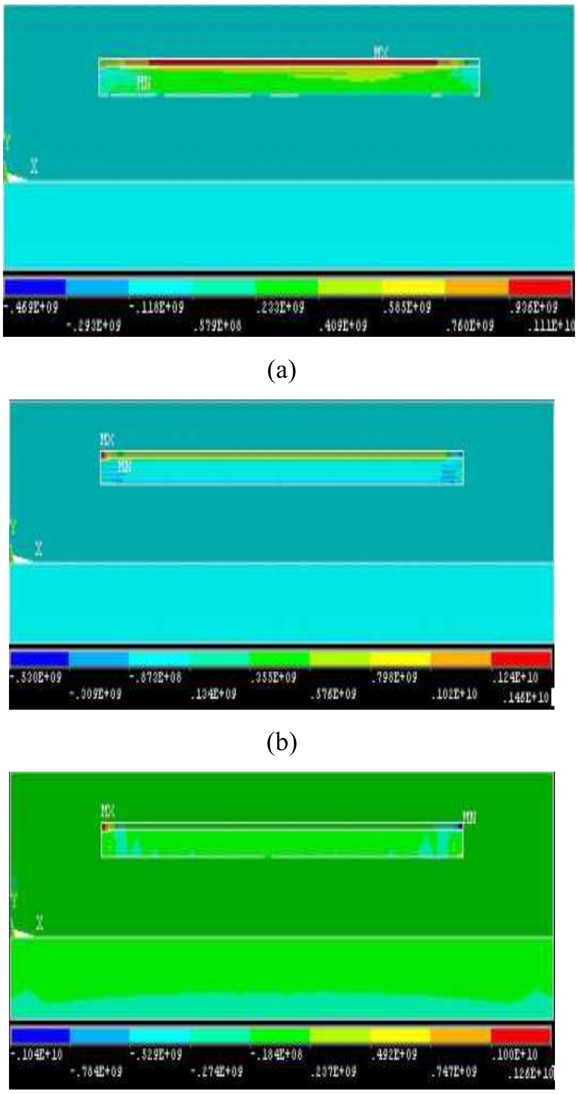

(a)

(b)

(c)

Fig. 5. Reverse direction of scanning of stress distribution; (a) *X* stress distribution; (b) *Y* stress distribution; (c) *Z* stress distribution.

b) Stress in three directions under the reverse direction of scanning method.

Fig. 5 shows the stress distribution in the *X*, *Y*, and *Z* directions of the thin-walled layer under reverse direction scanning. In Fig. 5(a), the stress concentration is observed in the middle with a tensile stress along the scanning direction (from left to right) and stress values ranging from about 200 MPa to 500 MPa. Fig. 5(b) shows a quite uniform stress distribution with stress values ranging from about -100 MPa to -20 MPa at both ends and the middle of the thin-walled part. Similarly, in Fig. 5(c), a uniform stress distribution is observed on the thin-walled part, where the stress tends to increase along the height from compressive stress to tensile stress with stress values ranging from about -100 MPa to 10 MPa. The stress in the *X* direction is dominant and higher than the stress in the *Y* and *Z* directions, indicating that the main stress is in the *X* direction.

3. Experimental Procedure

The DLMD forming system, as illustrated in Fig. 6, comprises a 0.5 KW Fiber laser, powder feeder, powder nozzle, and a three-axis linkage workbench. In this experiment, inconel 625 super alloy powder was utilized, with a particle size ranging from 15 to 55 µm, as presented in Table 1. Fig. 7 displays micrograph of Inconel 625 powder under Hitachi S-3000N Scanning Electron Microscope.

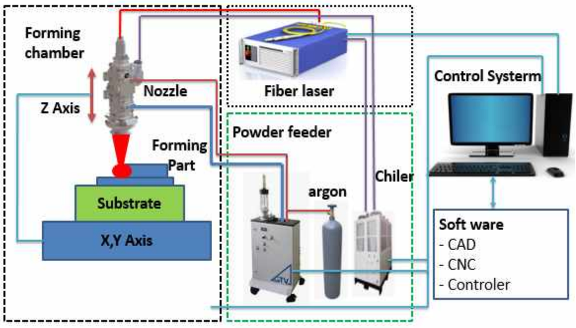

Fig. 6. DLMD system schematic.

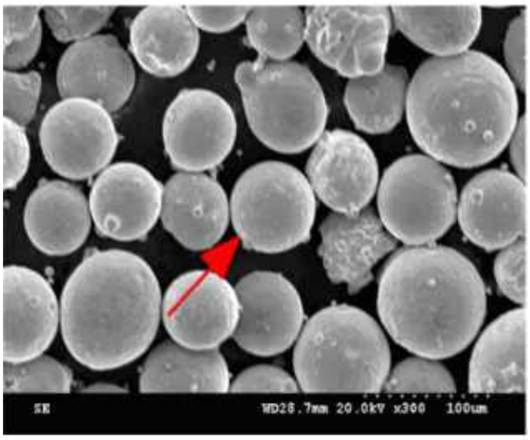

Fig. 7. SEM micrograph of Inconel 625 powder.

Table 4. Samples and dimension

No	Nozzle travel path strategies	Dimension (mm)	Layer numbers
No1	Single direction of scanning	40×0.5×10	100
No2	Reverse direction of scanning	40×0.5×10	100

The substrate material was 316L stainless steel, with a geometric dimension of 100 mm × 500 mm × 10 mm and composition indicated in Table 2. The thin wall component with dimensions of 40 mm × 0.5 mm × 10 mm is formed using two nozzle scanning methods, simples as demonstrated in Table 4, process parameters as Table 3. Prior to the experiment, the metal powder was dried in a vacuum drying oven at 200 °C for 4 hours to eliminate moisture. The substrate was polished with sandpaper and then cleaned with acetone and ethanol to remove grease and stains. Following the finalization of the forming process, the thin walls undergo precision cutting via an electrical discharge wire, yielding petite samples portrayed in Fig. 8(a) and Fig. 9(a). Subsequently, these samples are meticulously polished and subjected to scrutiny beneath an electron microscope, as illustrated in Fig. 8(b,c,d) and Fig. 9(b,c,d), in order to detect any visible fissures. Samples exhibiting signs of fractures are subjected to thorough examination through Scanning Electron Microscopy (SEM) to elucidate the nuances of the crack morphology. Furthermore, an electron optical microscope is employed for a comprehensive investigation of the microstructural aspects of these samples. Following these analytical steps, the specimens undergo a rigorous hardness assessment using the Duramin hardness testing machine.

4. Results and Discussions

4.1. Crack Morphology

To investigate the impact of stress distribution on crack occurrence and warping in the cladding layer, experiments were conducted, and the findings are presented in Fig. 8 and Fig. 9. These figures illustrate samples of a thin-walled part made from Inconel 625, which was formed using DLMD with various scanning modes.

Fig. 8 shows that the first sample, which was formed using the single direction of scanning method, had a greater number and size of cracks in the middle layers compared to those at the two ends of the thin-walled part. On the other hand, Fig. 9 shows that the second sample, formed using the reverse direction of scanning method, had not cracks at both ends and in the middle of the thin-walled part. This can be attributed to the large concentration of stress in the middle of the thin-walled part and the lower stress at both ends that is evident in the simulated stress results for the single direction of scanning method. Thus, when the stress exceeds the tensile strength of the material, cracks will appear. Conversely, under the reverse direction of scanning method, the stress is lower, so no cracks appear during the forming process of the thin-walled part.

Fig. 10 displays magnified images of a crack captured under Hitachi S-3000N Scanning Electron Microscope. Fig. 10(a) shows a close-up of the crack, and Fig. 10(b) provides a detailed view of the crack mouth. Notably, Fig. 10(b) reveals bright areas on the oxidized crystal and columnar structure on the surface of the crystal, with a liquid layer coating the top. This indicates that the crack formed due to high-temperature conditions, and the crystal boundaries were separated by liquid layers. Thus, the observed crack is a typical sample of a hot crack.

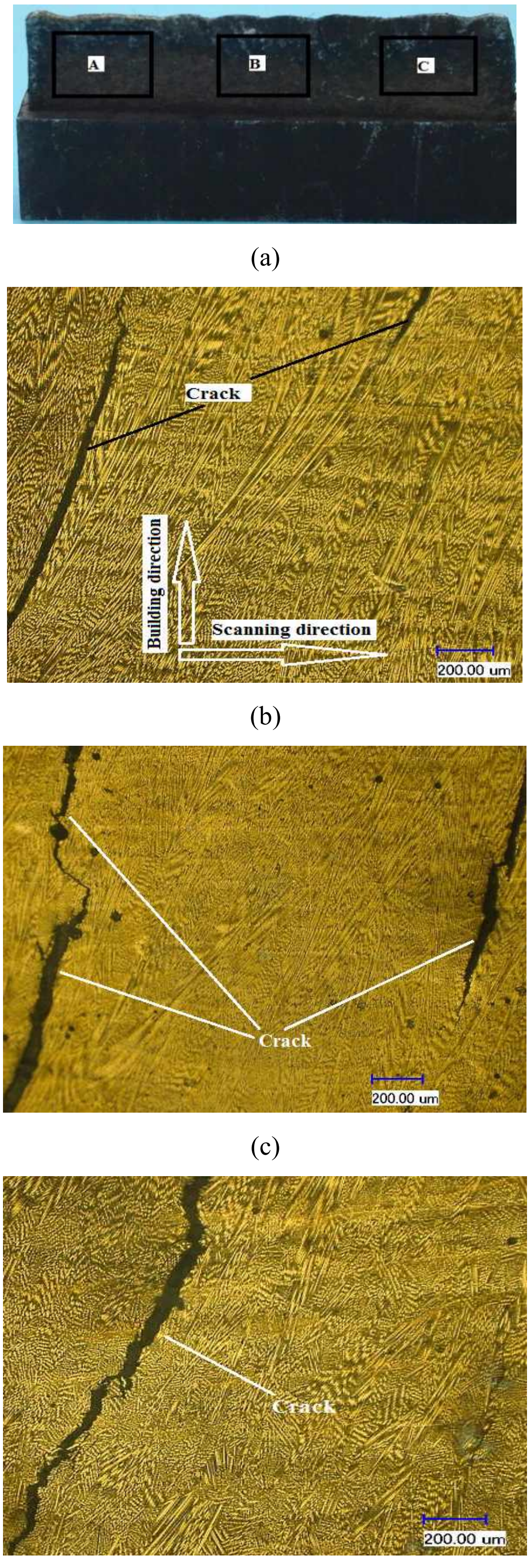

(a)

(b)

(c)

(d)

Fig. 8. Images of the experimental sample formed by using single direction of scanning method and the corresponding optical microscope images of areas A, B, and C on the formed sample. (a) Sample No1; (b) Area A; (c) Area B; (d) Area C.

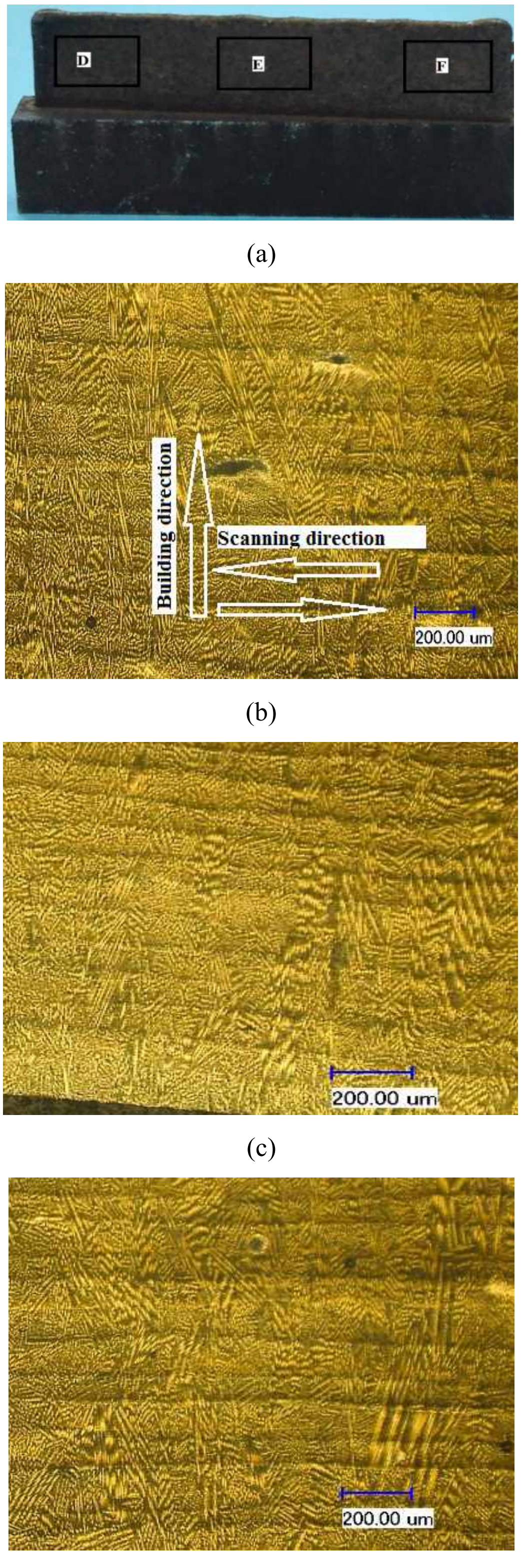

(a)

(b)

(c)

(d)

Fig. 9. Images of the experimental sample formed by using reverse direction of scanning method and the corresponding optical microscope images of areas D, E, and F on the formed sample. (a) Sample No2; (b) Area D; (c) Area E; (d) Area F.

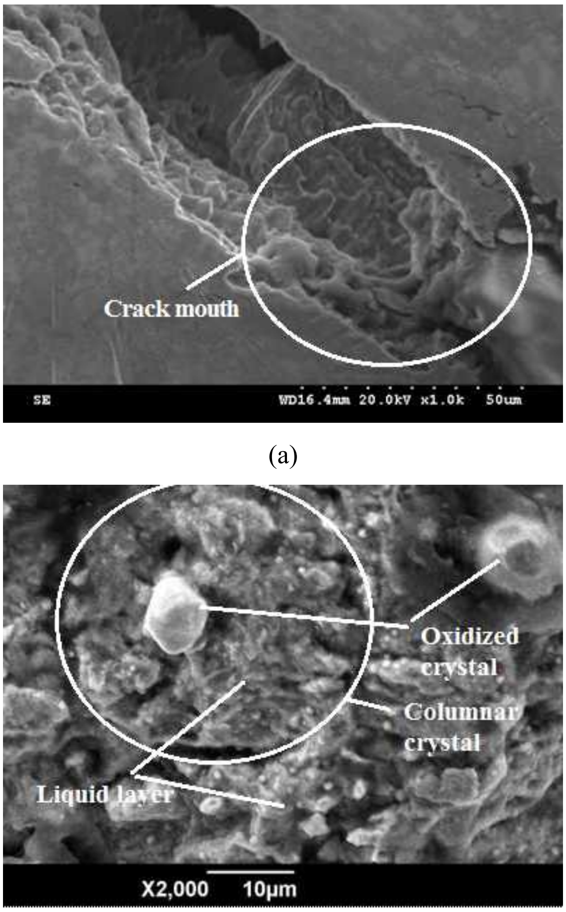

(a)

(b)

Fig. 10. The SEM images of crack on the component: (a) The crack morphology; (b) Image of the crack mouth.

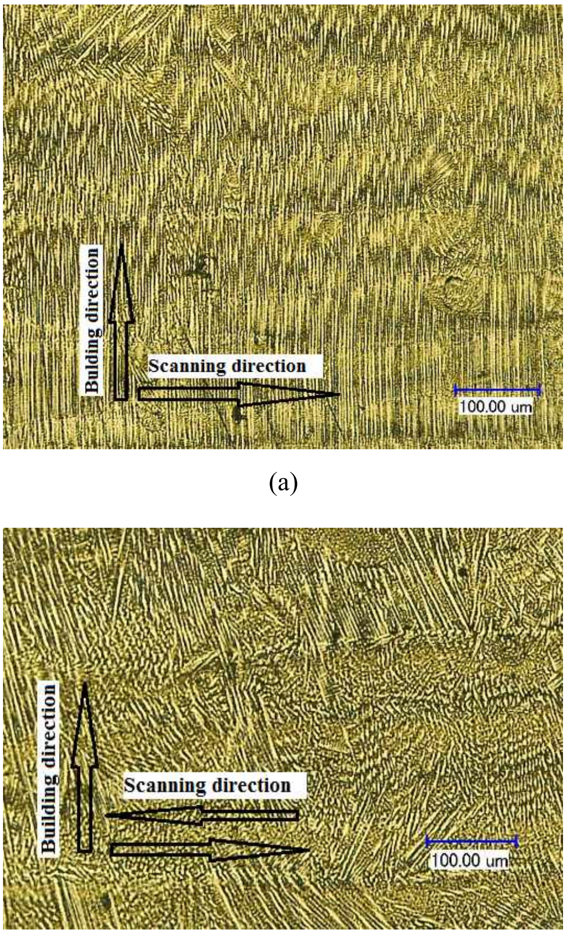

(a)

(b)

Fig. 11. Microstructure images of the part shaped in the vertical plane using (a) single direction of scanning and (b) reverse direction of scanning.

The DLMD is technology utilizing a unique process where the shaping material is rapidly heated to a molten state, followed by a fast cooling process during crystallization. When subjected to a high-energy laser beam, the metal area and its surroundings reach an extremely high temperature and partially melt, causing the affected material area to expand and undergo compressive stress, which is constrained by neighboring areas. This results in a decrease in stress value as the temperature increases. However, the stress value at the center of the molten area may exceed the allowable limit, leading to plastic deformation under elastic deformation.

During the crystallization process, the constrained molten area is subjected to tensile stress as it is not free to shrink and must be confined by surrounding areas. The extremely fast cooling rate, causes an uneven distribution of chemical components, resulting in high melting point elemental clusters crystallizing before low melting point ones. This leads to liquid membranes separating from the crystal cluster boundary, which creates cracks. Due to the columnar crystal structure of the DLMD material, these cracks tend to develop along the boundary between crystal clusters.

In summary, the DLMD shaping technology rapidly heats and cools the shaping material, causing compressive and tensile stresses. Uneven distribution of chemical components during crystallization leads to crack formation. The columnar crystal structure of DLMD material causes cracks to develop along crystal cluster boundaries.

4.2. Microstructure

An important characteristic of Inconel 625 alloy material when shaped using DLMD technology is the presence of very small, long, vertically developed columnar crystal structures, as illustrated in Fig. 11. This is due to the rapid crystallization rate and large temperature gradient, resulting in small and uniform crystal structures. The crystallization process occurs at the boundary surface between the solid and liquid phases, ensuring that the liquid and solid phases remain in contact throughout the entire process. This type of crystal structure is typical of columnar crystals. Fig. 11(a) also depicts the continuous bonding between the shaped layers, which not only enhances the material's mechanical properties but also ensures the continuous development of crystal structures between the layers.

Fig. 11(a, b) illustrate the microstructure of the parts shaped using the single direction of scanning and reverse direction of scanning methods, respectively. The microstructure of the two basic samples is quite similar, featuring a columnar structure. The part shaped using the single direction of scanning method exhibits a continuously developed columnar crystal structure between the shaped layers, with long crystal lengths and vertical development along the height of the shaped layers, showed in Fig. 11(a). On the other hand, the part shaped using the reverse direction of scanning method also has a columnar crystal structure, but the development direction is oblique, with shorter crystal lengths and no continuous development between the shaped layers, showed in Fig.11(b).

According to the rapid solidification theory, the microstructural dimension depends on the cooling speed. The cooling speed V can be expressed as [13]:

$$V = G \times R \qquad (6)$$

where the G is the temperature gradient and R is the solidification rate.

Regarding the single direction scanning method, the beginning scanning time for the second layer is longer because the nozzle needs to return to its initial position, leading to a significant reduction in the temperature of the first layer and a larger temperature gradient between the two layers. Consequently, the cooling rate (V) is high, and heat transfer occurs from the top layer to the bottom layer, resulting in the formation of a cylindrical crystal structure with vertical development.

In contrast, the reverse direction scanning method does not have idle time for the nozzle, allowing the top layer to take shape earlier while the bottom layer has not fully cooled. As a result, the temperature gradient between the two layers is smaller, and the cooling rate (V) is lower. Heat transfer occurs to both sides of the wall, leading to the development of obliquely oriented cylindrical crystal structures. The cross-sectional views of the parts shown in Fig.11(a) and (b) demonstrate columnar crystal structures with small, relatively uniform grain sizes of around 5÷7 micrometers.

4.3. Microhardness

Two thin wall parts have been sectioned into small samples that correspond to areas A, B, C, D, E, F as illustrated in Fig. 8(a), 9(a), and 12(a). The hardness of each of these small samples is measured using a Duramin versatile hardness tester. Fig. 12(c) depicts the measurement diagram where row 1 corresponds to the bottom layer, row 2 represents the middle area, and row 3 depicts the top area of the thin component. The measuring position of a point is located at the center of the formed layer, as demonstrated in Fig. 12(b).

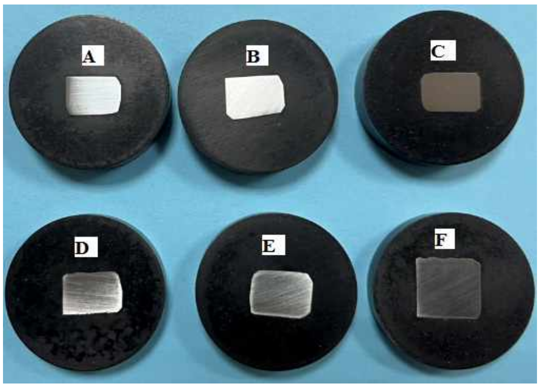

(a)

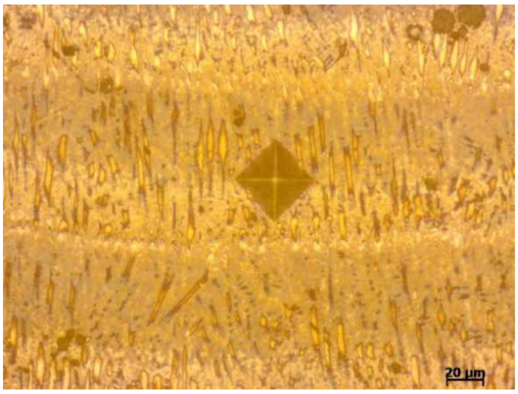

(b)

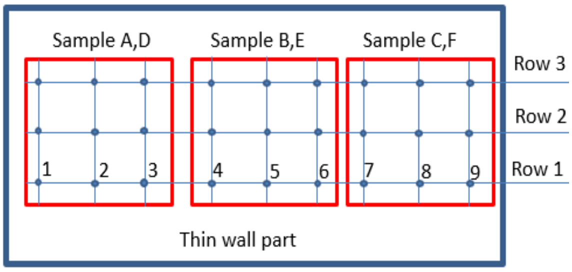

(c)

Fig. 12. Microhardness measurement samples and position: (a) Images of the samples were cut from two thin wall parts; (b) Measurement trace image by Duramin versatile hardness tester; (c) Measurement position on samples.

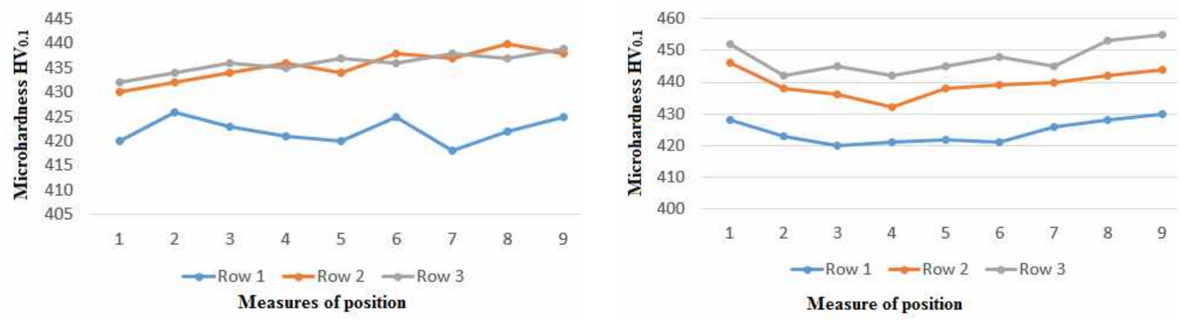

(a) (b)

Fig. 13. Microhardness measurement results of two thin wall parts. (a) The measurements result performed on samples A, B, and C; (b) The measurements result performed on samples D, E, and F.

Fig. 13(a) shows the microhardness measurement values at positions on samples A, B, and C of thin wall part 1, corresponding to the part formed by the single direction of scanning method. Fig. 13(b) shows the microhardness measurement values at positions on samples D, E, and F of thin wall part 2, corresponding to the part formed by the reverse direction of scanning method. The results indicate that, in both cases, the microhardness increases with the height of the formed layers; the microhardness values in the left, right, and middle areas are relatively uniform. For part 1, the microhardness measurement values range from 420 to 435 HV. For part 2, the microhardness measurement values range from 420 HV to 450 HV.

During the shaping process, heat accumulation causes the temperature of the molten pool in the upper layers to gradually increase. This leads to the overflow of molten material to both sides, reducing the height of the shaping layer and increasing material density. Consequently, microhardness also gradually increases. Once the height of the shaping layer reaches a certain value and heat accumulation stabilizes, the temperature of the molten pool stops increasing. This stabilizes the thickness of each layer and results in the microhardnes reaching a stable state with no further increase. Although there are differences in the distribution of microhardness in both cases, the changes are not significant.

5. Conclusion

The paper investigated the influence of two distinct scanning methods on the temperature field, stress field, crack formation, microstructure, and microhardness of a thin component fabricated using DLMD. The scanning method had a significant impact on both the magnitude and distribution of stress within the component, leading to crack formation in the two distinct components. Furthermore, the scanning method also affected the temperature field, resulting in noticeable variations in the microstructure and microhardness between the two components.

Under the single direction of scanning method, cracks are often observed in the middle of the thin-walled parts, with severe cracking at both ends. The direction of cracking is generally perpendicular to the main stress direction. In contrast, under the reverse direction of scanning method, no cracks are typically observed within the thin-walled parts and no cracking occurs at either end.

The microstructure of the Inconel 625 material in the forming layer is characterized by a columnar crystal structure that has a small length and grows perpendicularly to the scanning direction. This growth is continuous between the forming layers.

In both cases, the microhardness increases with the height of the formed layers; the microhardness values in the left, right, and middle regions are relatively uniform, the microhardness measurement values range from 420 HV to 450 HV.

Acknowledgments

This research is funded by Vietnam National Foundation for Science and Technology Development under grant number KC4.0-15/19-25.

References

[1]. G. Jie *et al*., Effect of Nb content on microstructure and corrosion resistance of Inconel 625 coating formed by laser cladding, Surface and Coatings Technology, Vol. 458, pp.2023. https://doi.org/10.1016/j.surfcoat.2023.129311

[2]. G. Adrian Grabos *et al.* Thermal properties of Inconel 625-NbC metal matrix composites (MMC), Materials & Design Vol 224, 2022. https://doi.org/10.1016/j.matdes.2022.111399

[3]. C. Fei *et al*, Microstructures and mechanical behaviors of additive manufactured Inconel 625 alloys via selective laser melting and laser engineered net shaping, Journal of Alloys and Compounds, Vol. 917, 2022. https://doi.org/10.1016/j.jallcom.2022.165572.

[4]. R. Duqiang, X. Zhiyuan, *et al*. Zhang, Influence of single tensile overload on fatigue crack propagation behavior of the selective laser melting inconel 625

superalloy, Engineering Fracture Mechanics, Vol. 239,2020, https://doi.org/10.1016/j.engfracmech.2020.107305.

[5]. Zh. Lin, C. Suiyuan, Zh. Chenyi Zhang, *et al*,. Microstructure evolution and properties of direct laser deposited 24CrNiMoY alloy steel assisted by non-contact ultrasonic treatment, Materials Science and Engineering: A, Vol. 811,2021, https://doi.org/10.1016/j.msea.2021.141088.

[6]. N. Shamsaei, Aref. Yadollahi, *et al*,. An overview of Direct Laser Deposition for additive manufacturing; Part II: Mechanical behavior, process parameter optimization and control, Additive Manufacturing, Vol. 8,2015. https://doi.org/10.1016/j.addma.2015.07.002.

[7]. Zia. Ullah Arif, Muhammad Yasir Khalid, Ehtsham ur Rehman, Laser-aided additive manufacturing of high entropy alloys: Processes, properties, and emerging applications, Journal of Manufacturing Processes, Volume 78, pp 131-171, 2022 https://doi.org/10.1016/j.jmapro.2022.04.014.

[8]. Zh. Lin, Ch. Suiyuan, *et al.* Microstructure and properties of 24CrNiMoY alloy steel prepared by direct laser deposited under different preheating temperatures, Materials Characterization, Vol. 158, 2019, https://doi.org/10.1016/j.matchar.2019.109931.

[9]. Li. Shihua, Chen. Bo, Tan. Caiwang, Song. Xiaoguo, Effects of oxygen content on microstructure and mechanical properties of 18Ni300 maraging steel manufactured by laser directed energy deposition, Optics & Laser Technology, Vol. 153, 2022, https://doi.org/10.1016/j.optlastec.2022.108281.

[10]. https://www.metalpowder.sandvik/49f42c/siteassets/metal-powder/datasheets/osprey-alloy-718-am-viga.pdf

[11]. https://d2zo35mdb530wx.cloudfront.net/_legacy/UCPthyssenkruppBAMXUK/assets.files/material-data-sheets/stainless-steel/stainless-steel-1.4404-316l.pdf

[12]. Ehsan. Foroozmehr, Radovan. Kovacevic. Effect of path planning on the laser powder deposition process: thermal and structural evaluation, Int J Adv Manuf Technol, Vol. 51, 2010, pp:659–669.

[13]. Yongjun Huang, Xiaoyan Zeng. Investigation on cracking behavior of Ni-based coating by laser-induction hybrid cladding. Applied Surface Science, 256, 5985-5992, 2010.